Velocity Imaging of Highly Turbulent Gas Flow

Benedict Newling,[1,*] Christopher C. Poirier,[1] Yang Zhi,[1] James A. Rioux,[1] Andrew J. Coristine,[1,†] Dale Roach,[2] and Bruce J. Balcom[1]

[1]*MRI Centre, Department of Physics, University of New Brunswick, P.O. Box 4400, Fredericton, New Brunswick, Canada NB E3B 5A3*

[2]*Department of Engineering, K.C. Irving Hall, University of New Brunswick, Saint John, New Brunswick, Canada*

(Received 17 March 2004; published 5 October 2004)

We introduce a noninvasive, quantitative magnetic resonance imaging (MRI) wind-tunnel measurement in flowing gas ($>10\ \mathrm{m\,s^{-1}}$) at high Reynolds numbers ($\mathrm{Re} > 10^5$). The method pertains to liquids and gases, is inherently three dimensional, and extends the range of Re to which MRI is applicable by orders of magnitude. There is potential for clear time savings over traditional pointwise techniques. The mean velocity and turbulent diffusivity of gas flowing past a bluff obstruction and a wing section at realistic stall speeds were measured. The MRI data are compared with computational fluid dynamics.

DOI: 10.1103/PhysRevLett.93.154503 PACS numbers: 47.27.–i, 47.17.+e, 47.80.+v, 87.61.–c

Introduction.—Most engineering and naturally occurring flows are turbulent. Measurements of such flows are critical in a variety of arenas from aircraft design to predicting climate change. Magnetic resonance imaging (MRI) holds much promise for the study of turbulent flows, because the method is completely noninvasive, does not require that the flowing substance be optically transparent, and because the MRI signal can be acquired from the entire flow field simultaneously and does not require point-by-point measurements, e.g., [1–3]. Until now, MRI has been largely limited to fluid speeds $\sim 1\ \mathrm{m\,s^{-1}}$, with a few notable exceptions slightly in excess [4,5].

A new combination of purely phase-encoded MRI methods (e.g., [6]) with flow sensitization has allowed us to develop a wind-tunnel style MRI measurement. It is possible to generate purely phase-encoded images with no signal cancellation over a much greater range of fluid speeds and, hence, Reynolds numbers than with conventional MRI methods due to a short characteristic time interval of the measurement (see below). From this baseline, a novel motion-sensitized version of the phase-encoded method (single-point ramped imaging with T1 Eenhancement) was used to add turbulence-based image contrast in a controlled fashion. The method realizes, for the first time, the possibility of a completely noninvasive velocity and turbulence intensity quantification by MRI at flow rates and Reynolds numbers (Re) which are broadly relevant. The entire spin system can be interrogated by every acquisition, which suggests considerable advantages in information per unit acquisition time over other wind-tunnel measurements. In addition, purely phase-encoded methods are applicable to a broader range of fluids than conventional MRI, which is usually restricted in studies of turbulent flow to liquids with long-lived MRI signals ($\sim 10^{-2}$–10^{1} s). Many gas MRI signals [7] are short-lived ($\sim 10^{-4}s$–10^{-2} s) [8].

Materials and methods.—Measurements were made using a Nalorac (Martinez, USA) 2.35-T, horizontal-bore superconducting magnet and Tecmag (Houston, USA) Apollo console. A water-cooled 7.5-cm-i.d. Nalorac magnetic field gradient set was driven by Techron (Elkhart, USA) 8710 amplifiers. All measurements were performed using a home-built, quadrature, birdcage radio frequency (rf) coil, driven by a 2-kW AMT (Brea, USA) 3445 rf amplifier. Gas flow was driven around a closed loop of cylindrical pipe through the center of the magnet, gradient set and rf coil by a centrifuge pump (Ametek Lamb Electric, Kent, USA). The loop was filled with sulfur hexafluoride (SF_6) and the displaced air was exhausted through an outlet on the opposite side of the loop. Water could have yielded similar Re at lower flow speeds (by a factor of 2.5), but the gas was relatively easy to pump at speed. We do not demonstrate compressible flows here, but the choice of SF_6 makes measurement in compressible flows a possibility. Independent measurement of mean fluid speed was performed using a Venturi flow meter. During filling, a bulk ^{19}F signal was acquired until a maximum was reached. SF_6 is approximately 5 times denser than air ($5.69\ \mathrm{kg\,m^{-3}}$ at 315 K and 0.1 MPa). The viscosity is 1.6×10^{-5} Pa s at 315 K [11,12]. All images presented are of ^{19}F. Bulk values of $T_1 = T_2 = 1.4$ ms were measured at 0.1 MPa [6]. The section of pipe through the magnet is a replaceable test section, in which a variety of obstacles have been studied. Images of two test sections are included here: a bluff obstruction and a Clark-Y wing section. Both were 44 tube diameters downstream of the Venturi meter to allow flow development before the obstruction. The wing was shaped from expanded polystyrene foam and encased in Mylar film (Monokote, Top-Flite, USA).

MRI relies upon the acquisition of magnetic resonance signal in the presence of a magnetic field gradient to impart a spatial dependence upon the signal

$$s(\vec{k}) = \int \rho(\vec{r}) \exp(-i2\pi\vec{k}\cdot\vec{r}) d\vec{r} \left[\vec{k} = \frac{\gamma}{2\pi} \int \vec{G}(t) dt \right], \quad (1)$$

where s is the MRI signal, ρ is the distribution of nuclear spins (^{19}F), $\vec{r}$ is a position vector, and the integral is over all space. For ^{19}F, the magnetogyric ratio $\gamma = 25.18 \times 10^7$ rad s^{-1} T^{-1}. The distribution of spins (the image) is the Fourier transform of the signal $S(\vec{k})$. Most MRI methods acquire digitized samples of $S(\vec{k})$ in a constant magnetic field gradient [$\vec{G}(t) = \vec{G}$] after each rf excitation. This approach is termed *frequency encoding*. Typical frequency encoding techniques (*spin-warp* methods [13]) are prone to generate images weighted by local variations in signal lifetime and have limited the flow regimes which have been studied by MRI. Turbulent flow causes signal cancellation in such images, except in flow fields with moderate Re or where reduced $\vec{k}$-space sampling schemes are employed [3]. Purely *phase-encoded* imaging methods, in contrast, acquire a single data point at a constant interval, $t = t_p$, after each of many separate excitations. $\vec{G}$ is changed with each acquisition. t_p can be made sufficiently short compared to the signal lifetime of most materials that true spin density images may be acquired. We demonstrate here that phase-encoded methods are robust for the imaging of turbulent fluid flow.

Data were acquired with a new, motion-sensitized version of the phase-encoding method. The standard (method A [14], with constant gradient G during t_p) is compared with the new variant (method B) in Fig. 1. The primary phase-encoding gradient in method B was switched from $G - g$ to $G + g$ during the interval t_p. The zeroth gradient moment with respect to time, over t_p, is the same as that of method A. For a moving sample, we expand the $\vec{r}$ of Eq. (1) as a Taylor series. Initial position information is encoded by the zeroth gradient moment, velocity by the first moment, and so on to higher orders.

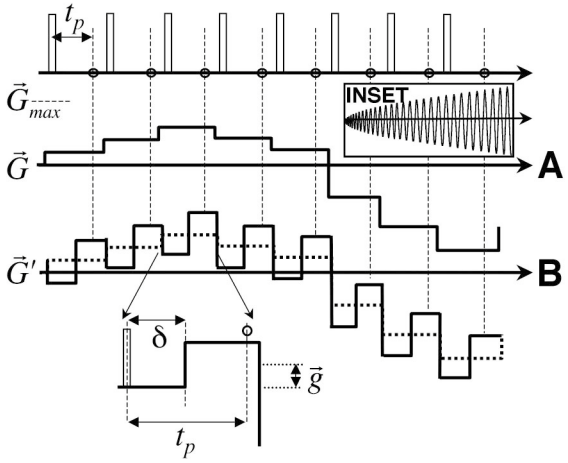

FIG. 1. Schematic of the magnetic field gradients used in the primary phase encode direction for imaging. Method A shows the first few gradient values of the 2564-point spiral trajectory (inset) [14]. Method B shows the motion-sensitized version of that trajectory. The upper line is the history of rf application and data acquistion. One phase-encoded data point is acquired at each circle, at a time t_p after rf pulse application. $\vec{G}'$ differs from $\vec{G}$ only in a symmetrical excursion ($\vec{g}$) either side of $\vec{G}$. The superposition of $\vec{g}$ excursions upon any $\vec{k}$-space sampling scheme is possible.

$$2\pi\vec{k}\cdot\vec{r}(t) = \vec{r}(0)\int \vec{G}(t)dt + \dot{\vec{r}}\int \vec{G}(t)t dt + \frac{1}{2}\ddot{\vec{r}}\int \vec{G}(t)t^2 dt \ldots. \quad (2)$$

Methods A and B have the same sensitivities to initial spin position, but different sensitivities to velocity, etc., which depends upon the size of g (Fig. 1). Several images were acquired using method B, with different values of g and, hence, different sensitivities to motion. With careful data analysis (see below), the series of images becomes a *map* of mean velocity and of turbulent diffusivity for the quantification of turbulent flows. In practice, any $\vec{k}$-space raster can be motion sensitized by the superposition of bipolar gradients in the encoding interval in one or more gradient directions. The images shown here have all been acquired with a acquisition scheme in which the center of $\vec{k}$ space ($\int \vec{G}dt = 0$) is sampled first [14]. The history of the primary phase-encoding gradient is shown in Fig. 1. This approach to velocity sensitization is not new [13], but the integration with the technique is. Where flows are rapid and turbulent, the new method confers important advantages over spin-warp frequency-encoded techniques (see Discussions and conclusions).

Results.—Instantaneous velocity $\vec{u}(t)$ for a fluid element may be decomposed into $\vec{u}(t) = [\overline{U}_1 + u_1(t)]\hat{x} + [\overline{U}_2 + u_2(t)]\hat{y} + [\overline{U}_3 + u_3(t)]\hat{z}$, where $\overline{U}_i$ ($i = 1, 2, 3$) are the time-averaged mean velocities in the x, y, and z directions, respectively, and $u_i(t)$ are the time varying parts of each velocity component (turbulent velocity fluctuations). The z axis is taken to lie along the magnet bore (with the mean flow). The MRI data contain information about both mean and fluctuating velocities. Herein, the velocity-sensitising gradient was applied in the z direction, with the principal phase-encoding gradient. The velocity-sensitizing gradient is readily chosen to lie along *any* direction by linear combination of x, y, and z gradients. This is an extremely powerful measurement tool in anisotropic systems.

Figure 2 shows the flow past an abrupt step obstruction in the test section. The mean flow speed in the unoccluded pipe was 17.0 m s^{-1} (Mach 0.12). In the unoccluded tube (diameter 3.4 cm), Re was 210 000. Eight images were obtained of SF_6 gas flowing past this bluff obstruction. Images were obtained by Fourier transformation of a

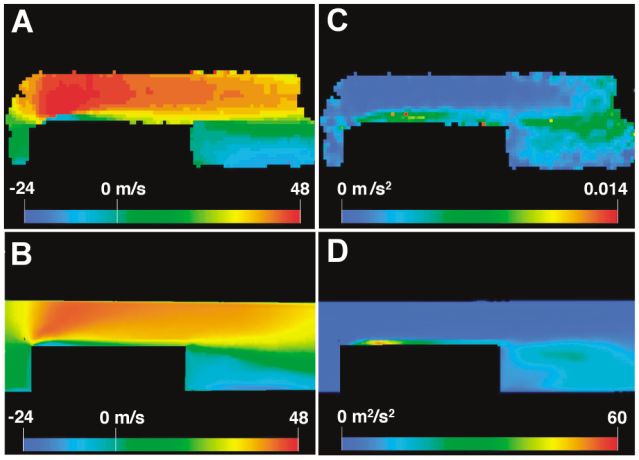

FIG. 2 (color). Bulk flow of gas is left to right in each image; the images are sensitized to the z component of fluid velocity. (a) MRI map of $\overline{U}_3$, derived from the g dependence of phase at each image voxel. Eight images acquired with different values of g were zero filled and Fourier transformed to give velocity quantification in 64 bins, each of width 3 m/s. (b) Computational fluid dynamics (CFD) map of $\overline{U}_3$ for an inlet condition of uniform mean velocity 17 m/s $\hat{z}$. (c) MRI map of D_{est} is derived [Eq. (4)], from images of stationary and flowing gas with $g = 10.2\ \text{mT m}^{-1}$. (d) CFD map of turbulence kinetic energy ($\langle u(t)^2\rangle/2$), which is related to (c) through Eq. (3). In all images, velocities outside the range of the scale bar are colored like the maximum or minimum.

64×64 array of $\vec{k}$-space data, which were zero filled to 96×96 voxels and apodized with a Hanning window function. Each image was acquired with a different value of g (Fig. 1, $g = 0$ to $g = 10.2\ \text{mT m}^{-1}$). $\delta = 300\ \mu$s for all images. The images were zero filled to 64 points before Fourier transformation in the third dimension, to give a data set with two spatial dimensions and one displacement dimension (64 images) [13]. Knowing δ, it is common practice to interpret these data as a z-velocity spectrum at each voxel [13]. Each image constituted a mean velocity bin of width $2\pi(n_g - 1)/\gamma\delta^2 N g_{\text{max}}$, where $n_g = 8$ is the number of motion-sensitizing gradient steps, $g_{\text{max}}/(n_g - 1) = 1.45\ \text{mT m}^{-1}$ is the increment in g, and $N = 64$ is the number of points to which the data were zero filled. For $\delta = t_p/2.0 = 300\ \mu$s the velocity spectral width is $192\ \text{m s}^{-1}$ and the interpolated velocity resolution of the images is $192/N = 3\ \text{m s}^{-1}$. Values for $\overline{U}_3$ were assigned to each voxel based upon the location of the peak in the z-velocity spectrum to generate a map of $\overline{U}_3$ [Fig. 2(a)]. The general form of the flow field in the CFD simulation of Fig. 2(b) corresponds very well to that which has been measured, giving confidence in the simulation.

The width of the z-velocity spectrum reflects the distribution of velocities at each voxel. In turbulent flow, the distribution is a measure of the velocity fluctuations during the measurement interval, which may be related to a turbulent (or eddy) diffusivity, D_t, in homogeneous turbulence by [15]

$$D_t = \langle u(t)^2\rangle T_{c_L}, \tag{3}$$

where T_{c_L} is the Lagrangian correlation time. The diffusivity was estimated on a voxel-by-voxel basis from

$$D_{\text{est}}(\vec{r}) = \frac{\ln[s_s(\vec{r})] - \ln[s(\vec{r})]}{\gamma^2 M(2\delta)}, \tag{4}$$

where s is the amplitude of signal in each voxel of position $\vec{r}$ and s_s is the amplitude of signal in the same voxel when the fluid is stationary ($g = 10.2\ \text{mT m}^{-1}$ in both cases).

$$M(t) = \int_0^t \left[\int_0^{t'} \vec{G}(t'')dt''\right] \cdot \left[\int_0^{t'} \vec{G}(t'')dt''\right] dt'. \tag{5}$$

$1/[\gamma^2 M(t)]$ was $29.6\ \text{cm}^2/\text{s}$, taking both the z and y gradients to be the average of their absolute values during each image acquisition [16]. Figure 2(c) shows a map of turbulent diffusivity and a CFD-generated map of turbulence kinetic energy [$= \langle u(t)^2\rangle/2$] appears in Fig. 2(d).

The upper limit of T_{c_L} was estimated from nonspatially resolved measurements on the flowing gas [1], which suggest $T_{c_L} < 600\ \mu$s, even at a Re number of 130 000. Assuming that T_{c_L} decreases with increasing Reynolds number, $T_{c_L} \lesssim t_p$, therefore, in the flow field of Fig. 2. A distribution of T_{c_L}, which was roughly log normal centered near 100 μs (1 standard deviation spanning 70–200 μs), was calculated from Figs. 2(b) and 2(d) and Eq. (3). The correlation time must be imaged to obtain precise estimates of $D_t(\vec{r})$ [1], but t_p is everywhere $> 2T_{c_L}$ and so $D_{\text{est}}(\vec{r}) \approx D_t(\vec{r})$.

Figure 3 shows similar data for a Clark-Y aerofoil test section. The wing chord measured 36 mm. The aerofoil was placed inside the pipe at an angle of 10°. The mean Venturi-measured velocity was $12\ \text{m s}^{-1}$ (Mach 0.085) and the Reynolds number (from the chord length) 150 000. This flow regime represents a realistic scaled stall speed for the aerofoil. There is some discrepancy in

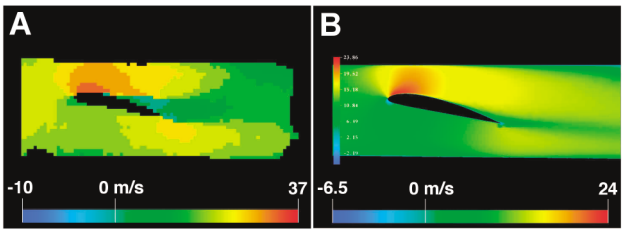

FIG. 3 (color). (a) MRI map of $\overline{U}_3$ and (b) corresponding CFD simulation of the flow field. The obstruction is a Clark-Y wing section of mean chord length 36 mm. The Venturi flow velocity was $12\ \text{m s}^{-1}$ giving a Reynolds number (based upon chord length) of 150 000. These represent realistic stall conditions.

the range of velocities measured in the MRI data and calculated in the CFD data (with an inlet velocity of $12\ \mathrm{m\,s^{-1}}\hat{z}$), which we impute to miscalibration of the Venturi meter (the steady-state temperature of the gas is lower for this obstruction than for the abrupt step).

Discussions and conclusions.—More typical measurements of velocity, such as hot wire anemometry, are made at a single point in space, but almost instantaneously. A time series of $\sim 10^3$ points is acquired to sample the statistics of the flow. The time series measurement is repeated at many points in the flow field to build up a map of the statistical behavior. In contrast, MRI can sample all spatial points in a shorter time, offering a time saving. We have less control over the time domain sampling, although there are MRI methods which capture snapshots of turbulent flow fields [17,18]. With our method, the whole of $\vec{k}$ space must be sampled before a two-dimensional image can be constructed (4 min), so there is intrinsic temporal averaging of the data over this interval. Mean velocities were extracted from $n_g = 8$ points in reciprocal displacement space, which imposes additional averaging. These data could be extracted from $n_g = 2$ data, an approach which is used in clinical imaging. Phase-encoded imaging methods offer potential in the study of fast fluid (gas or liquid) flows, because t_p can be made sufficiently short that fluid displacement in the encoding interval is reduced to manageable levels, when compared with the resolution of the image. At $17\ \mathrm{m\,s^{-1}}$ average fluid speed, the range of velocities and diffusivities present causes a smearing of the velocity maps. A point in the maps of velocity or diffusivity represents a point in a region within $\sqrt{2D_t t_p} \lesssim 4$ mm and $|\overline{U}_3(\vec{r})t_p| \leq 30$ mm upstream of its image location [16]. Adjustments to the gradient trajectory (to reduce the switching demands) will ensure that t_p and these uncertainties can be further reduced.

The short encoding interval permits images of turbulent flow, which show much reduced signal cancellation, compared with spin-warp techniques, to be acquired even when the turbulence intensity is high. This may be useful in some clinical contexts, to avoid signal voids downstream of stenoses, for example. Using the new method B, the turbulence-related contrast (intravoxel phase dispersion) may be added back into the image in a controlled fashion, to give a new quantitative insight. The bipolar gradient is the simplest form of motion sensitization; more sophisticated gradient applications will allow mapping of other properties of the flow field, such as velocity correlation functions [18,19]. In addition, the short encoding times permit samples with short T_2^* to be imaged. This makes the imaging of turbulent flows possible in a wider variety of fluids.

The combination of velocity sensitization with is new and furnishes the fluid mechanics community with a noninvasive measurement method, which can be implemented in a practical MRI wind tunnel. The range of relevant fluid speeds and Reynolds numbers measurable by MRI has been increased considerably by the new technique.

The authors thank the Natural Sciences & Engineering Research Council of Canada for assistance. The UNB MRI Centre is supported by NSERC. B. J. B. thanks the Canada Chairs program. B. N. thanks Professor L. D. Hall, Professor A. M. Hamza, and James Marshall for useful discussions.

*Electronic addresses: bnewling@unb.ca
http://www.unb.physics/mri
†Present address: Dept. of Med. Phys., University of Western Ontario, Ontario, Canada.

[1] D. O. Kuethe and J.-H. Gao, Phys. Rev. E **51**, 3252 (1995).
[2] J. Siegel, J. N. Oshinski, R. Pettigrew, and D. N. Ku, Magn. Reson. Med. **37**, 609 (1997).
[3] J. C. Gatenby and J. C. Gore, J. Magn. Reson. **121**, 193 (1996).
[4] K. S. Nayak, B. S. Hu, and D. Nishimura, Magn. Reson. Med. **50**, 366 (2003).
[5] H. M. Gach and I. J. Lowe, Magn. Reson. Med. **40**, 559 (1998).
[6] P. J. Prado, B. J. Balcom, I.V. Mastikhin, A. R. Cross, R. L. Armstrong, and A. Logan, J. Magn. Reson. **137**, 324 (1999).
[7] I.V. Koptyug, S. A. Altobelli, E. Fukushima, A.V. Matveev, and R. Z. Sagdeev, J. Magn. Reson. **147**, 36 (2000).
[8] There are exceptions, such as propane [9], butane, and hyperpolarized gases, for example, Ref. [10].
[9] S. L. Codd and S. A. Altobelli, J. Magn. Reson. **163**, 16 (2003).
[10] E. Brunner, M. Haake, L. Kaiser, A. Pines, and J. A. Reimer, J. Magn. Reson. **138**, 155 (1999).
[11] J. J. Hurly, D. R. Defibaugh, and M. R. Moldover, Int. J. Thermophys. **21**, 739 (2000).
[12] T. Strehlow and E. Vogel, Physica (Amsterdam) **161A**, 101 (1989).
[13] P. T. Callaghan, *Principles of Nuclear Magnetic Resonance Microscopy* (Oxford University Press, Oxford, 1991).
[14] M. Halse, D. J. Goodyear, B. MacMillan, P. Szomolanyi, D. Matheson, and B. J. Balcom, J. Magn. Reson. **165**, 219 (2003).
[15] J.-H. Gao and J. C. Gore, Med. Phys. **18**, 1045 (1991).
[16] D. O. Kuethe, Phys. Rev. A **40**, 4542 (1989).
[17] K. Kose, Phys. Rev. A **44**, 2495 (1991).
[18] A. J. Sederman, M. D. Mantle, C. Buckley, and L. F. Gladden, J. Magn. Reson. **166**, 182 (2004).
[19] A. A. Khrapitchev and P. T. Callaghan, J. Magn. Reson. **152**, 259 (2001).